

Representation of iron aerosol size distributions of anthropogenic emissions is critical in evaluating atmospheric soluble iron input to the ocean

Mingxu Liu^{1,2}, Hitoshi Matsui¹, Douglas Hamilton³, Sagar Rathod⁴, Kara Lamb⁵, Natalie Mahowald⁶

¹Graduate School of Environmental Studies, Nagoya University, Nagoya, Japan

²College of Environmental Science and Engineering, Peking University, Beijing, China

³Department of Marine, Earth, and Atmospheric Sciences, North Carolina State University, Raleigh, NC, USA

⁴La Follette School of Public Affairs, University of Wisconsin-Madison, Madison, WI, USA

⁵Department of Earth and Environmental Engineering, Columbia University, New York, NY, USA

⁶Department of Earth and Atmospheric Science, Cornell University, Ithaca, NY, USA

Correspondence to: M.L. (liumingxu@pku.edu.cn) and H.M. (matsui@nagoya-u.jp)

Abstract. Atmospheric aerosol deposition acts as a major source of soluble (bioavailable) iron in open ocean regions where it limits phytoplankton growth and primary production. The aerosol size distribution of emitted iron particles, along with particle growth from mixing with other atmospheric components, is an important modulator of its long-range transport potential. There currently exists a large uncertainty in the particle size distribution of iron aerosol, and the extent to which such uncertainty shapes global soluble iron deposition remains unclear. Here, we couple a sophisticated microphysical, size-resolved aerosol model with an iron-speciated and -processing module to disentangle the impact of iron emission size distributions on soluble iron input to the ocean, with a focus on anthropogenic combustion and metal smelting sources. We evaluate our model results against a global-scale flight measurement dataset for anthropogenic iron concentration and show that the different representations of iron size distribution at emission, as adopted in previous studies, introduces a variability in modeled iron concentrations over remote oceans of a factor of 10. Shifting the iron aerosol size distribution toward finer particle sizes (<1 μm) enables longer atmospheric lifetime (a doubling), promoting atmospheric processing that enhances the soluble iron deposition to ocean basins by up to 50% on an annual basis. The monthly enhancements reach 110% and 80% over the Southern Ocean and North Pacific Ocean, respectively. Uniquely, our results highlight that compared with emission flux variability, iron emission size distribution plays an equally important role in regulating soluble iron deposition, especially to the remote oceans. Our new findings can help to interpret inter-model differences in iron deposition estimation and to better quantify the effects of atmospheric nutrients input on marine biogeochemistry, including but not limited to iron, phosphorus, and others.

28 **1. Introduction**

29 Iron is a critical micronutrient supporting marine primary production, which is closely associated with marine carbon-nitrogen
30 cycles in the Earth system (Mahowald et al., 2018; Moore et al., 2001). The atmospheric deposition of soluble iron to many
31 ocean basins has long been regarded as an important source of bioavailable iron for ocean biota uptake in iron-limited areas
32 (Jickells et al., 2005; Jickells and Moore, 2015; Tagliabue et al., 2017). Understanding the amount and past-to-future evolution
33 of atmospheric iron deposition to the ocean is critical in assessing the ocean carbon sequestration under a changing climate
34 (Bergas-Massó et al., 2023; Myriokefalitakis et al., 2020; Hamilton et al., 2020b).

35 The quantification of soluble (bioavailable) iron input to the ocean is linked to differences in iron emission source properties,
36 the degree to which iron aerosol undergoes acidic or organic chemistry, and atmospheric transport (Hamilton et al., 2022).
37 Atmospheric iron comes from three major emission sources, i.e., wind-blowing dust, wildfire and biomass burning, and
38 anthropogenic activities, such as fossil fuel combustion and iron smelting. Dust storms, which frequently occur in arid or semi-
39 arid regions of the world, such as North Africa and East Asia, provide an abundant iron source to the ocean and support primary
40 production (Mahowald et al., 2009; Westberry et al., 2023). In addition, a growing body of evidence is showing that pyrogenic
41 iron, with higher fractional solubility than dust (Ito et al., 2019), is a large source of atmospheric soluble iron deposition to
42 many ocean basins, including the Southern Ocean, Northern Pacific Ocean, and Northern Atlantic Ocean (Conway et al., 2019;
43 Liu et al., 2022; Matsui et al., 2018; Seo and Kim, 2023). Because the strength of each source could be affected by future
44 climate change and/or human activities, their contributions to bioavailable iron input to the ocean may vary regionally and
45 temporally by the end of the century (Bergas-Massó et al., 2023).

46 Atmospheric transport provides the essential pathway in which iron aerosol emitted from the land is supplied to the remote
47 ocean. Atmospheric circulation patterns dictate the main transport pathways for aerosol to follow and thereby which source
48 regions are important to consider in terms of their supply to ocean basins. Additionally, atmospheric transport enables internal
49 mixing of iron-bearing aerosols with other aerosol and gas components, like sulfates and organics; a process commonly known
50 as aging that facilitates the dissolution of iron from an insoluble state to a soluble state (Shi et al., 2020; Shi et al., 2012;
51 Solmon et al., 2009; Li et al., 2017). The atmospheric aging processes can significantly increase iron solubility and subsequent
52 soluble iron deposition, evidenced by both in-field and laboratory observations and global model simulations (Ito, 2015; Li et
53 al., 2017; Longo et al., 2016). Uncovering the underlying mechanisms of the aging processes and associated enhancement of
54 iron solubility during transport is an ongoing topic of investigation (Meskhidze et al., 2019; Shi et al., 2020).

55 To elucidate atmospheric flux of iron-containing aerosols to the ocean, global-scale aerosol models have been developed to
56 include a range of iron emission sources that currently show a large intermodal difference in flux estimates (Myriokefalitakis
57 et al., 2018). Part of the problem is that it is difficult to realistically reproduce the distribution of soluble iron concentrations
58 across all the different regions of the world, and especially over the remote polar oceans that are often characterized by low
59 iron concentrations with a high fractional solubility (Ito et al., 2019). Among those global aerosol simulations, the size
60 distribution of iron, which is an important consideration when determining aerosol lifetimes and thus its long-range transport
61 potential, is key in shaping atmospheric iron distributions (Hamilton et al., 2020a; Myriokefalitakis et al., 2018). Compared to
62 coarse-sized particles (e.g., larger than 1 μm), smaller particles generally feature lower loss rates with respect to dry deposition
63 and wet removal, resulting in longer atmospheric lifetimes; being transported a longer distance increases the potential for
64 atmospheric processing (i.e., longer period of aerosol ageing) and thus higher soluble iron deposition. Evidence from recent
65 works (Zhang et al., 2023; Zhang et al., 2022) pointed out that Fe sources and physicochemical properties largely differ
66 between coarse and fine particles, leading to different Fe solubility. Representation of iron size distribution in models could
67 be therefore important.

68 Iron aerosol characteristics depend in part on differences between source types. The iron mass size distribution associated with
69 natural dust sources commonly pertains to mineral dust aerosols, with the coarse-sized (diameter greater than 1 μm) fraction
70 dominant (Mahowald et al., 2014; Albani et al., 2014). Similarly, fire iron emissions are dominated (>80%) by coarse mode
71 particles (Hamilton et al., 2019), suggested to be due to the entrainment of local dust iron-bearing aerosol in the pyro convective
72 updrafts generated by a fire (Hamilton et al., 2022). For iron aerosol with an anthropogenic source, however, the relative
73 fractions between the fine and coarse particle size distribution at emission are more divergent among previous investigations.
74 Recent observational constraints reveal large mass concentrations of anthropogenic iron oxide in the fine mode (Moteki et al.,
75 2017), while a subset of modelling studies have treated most of this iron in the coarse mode (Wang et al., 2015). As opposed
76 to those natural sources, anthropogenic iron size distributions may be highly variable with respect to diverse fuels, combustion
77 temperatures, and industrial processes, as well as the abatement technologies applied to control air pollution (Rathod et al.,
78 2020; Hamilton et al., 2020a).

79 The extent to which iron aerosol size distributions shape the pattern of atmospheric soluble iron inputs to different ocean
80 regions is currently unknown. Herein, by leveraging a size-resolved global aerosol model configured with iron processes, we
81 focus on the representation of anthropogenic iron size distributions at emission, primarily involving its roles in altering global
82 long-range transport and deposition fluxes of iron. We further put the effect of iron size distribution in the context with iron
83 emission uncertainty to shed light on their relative importance in controlling global-scale iron deposition.

84

85 **2. Methods and Materials**

86 **2.1 Global aerosol model**

87 We conducted global aerosol simulations using the Community Atmospheric Model version 5 (CAM5.3) with the Aerosol
88 Two-dimensional bin module for foRmation and Aging Simulation version 2 (CAM-ATRAS) (Matsui, 2017; Matsui and
89 Mahowald, 2017). The model treats a series of aerosol chemical and microphysical processes in a size-resolved manner with
90 12 aerosol size bins from 1 to 10,000 nm in diameter. Our recent study suggests that this size-resolved method can well
91 represent the growth of small particles to larger ones and the evolution of particle size distributions during atmospheric
92 transport (Liu and Matsui, 2022). Both dry deposition (Zhang et al., 2001) and wet deposition (Liu et al., 2012) of aerosols are
93 treated in our model. The improvement of aerosol in-cloud wet scavenging process was included to improve the modelling of
94 aerosol long-range transport efficiency (Liu and Matsui, 2021). The CAM-ATRAS model has been adequately validated for
95 aerosol mass and number concentrations at a global scale using comprehensive measurements from the ground to the upper
96 troposphere (Matsui and Liu, 2021; Gliß et al., 2021; Kawai et al., 2021; Matsui et al., 2022; Matsui and Moteki, 2020).

97 To represent the iron cycle from emission to deposition, we explicitly treated iron constituents within the aerosol model, similar
98 to our previous study (Liu et al., 2022), while with updates for iron processing in the current work. All iron-bearing components
99 were assumed to be internally mixed with other aerosols and underwent emission, physical transport, chemical aging (e.g.,
100 solubilization), and deposition in the atmosphere. The internal mixing assumption is reasonable for anthropogenic iron aerosols,
101 which are often mixed together with other aerosol compounds in the polluted environments, e.g., East Asia, and enable the
102 growth of iron aerosols via condensation and coagulation. Our model simulated iron solubility and atmospheric processing of
103 iron-bearing aerosols through the online coupling with the Mechanism of Intermediate complexity for Modelling Iron
104 (Hamilton et al., 2019). For anthropogenic iron, we consider five different minerals, namely magnetite, hematite, illite,
105 kaolinite, and sulfate iron, following the global emission inventory by Rathod et al. (2020), which was developed by a bottom-
106 up approach at 1° spatial resolution and 1-month temporal resolution. The reference year of the inventory was 2010. We
107 account for a wide range of anthropogenic sources including iron smelting and fossil fuel combustion sources.

108 Dust iron emission was calculated by assuming a constant iron content of 3.5% in dust aerosol emission (Shi et al., 2012). The
109 model estimated total dust emission fluxes using the scheme of Zender et al. (2003), with modifications by Albani et al. (2014)
110 and the size distribution from Kok (2011). Dust mineralogy was not involved in our simulations. The global interannual mean
111 iron (insoluble + soluble) emissions from dust, biomass burning, and anthropogenic sources were 87 Tg Fe yr⁻¹, 1.1 Tg Fe yr⁻¹,
112 and 2.2 Tg Fe yr⁻¹, respectively.

113 We validated our modeled anthropogenic iron oxide concentrations against a global-scale aircraft measurement in the
114 troposphere consisting of eight campaigns for the periods of 2009–2011 and 2016–2018 (Lamb et al., 2021). These
115 observations provide mass concentrations of anthropogenic iron oxide, i.e., magnetite, with volume equivalent diameters
116 between 180–1290 nm. The model results were extracted along the flight tracks in time and space and further averaged in
117 several latitudinal bands across Pacific and Atlantic Oceans (see Fig. S1). More details can be seen in Liu et al. (2022).

118 The model was compiled with a horizontal resolution of 1.9° × 2.5° (latitude × longitude) and 30 vertical layers from the
119 surface to 40 km. We ran the model for the two periods, 2008–2011 and 2015–2018, with the first year in each period as spin-
120 up. The meteorological fields were nudged by the Modern-Era Retrospective analysis for Research and Applications Version
121 2. In addition, to provide implications for ocean biogeochemistry, we estimated the changes in marine net primary production
122 induced by iron inputs following the methods used by Rathod et al. (2022) and Okin et al. (2011), in which a cut-off (4 μmol
123 L⁻¹) of nitrate concentrations at surface water was chosen to define the geographical areas of iron-limited ocean basins.

124 **2.2 Representation of iron size distribution of anthropogenic emissions**

125 The number and mass size distribution of aerosol at emission is an essential parameter in aerosol modelling. However, due to
126 the limited knowledge about iron emission characteristics, the representation of iron size distributions varies greatly for
127 anthropogenic sources. We tested four different size distributions of anthropogenic iron at emission (Fig. 1), briefly described
128 as follows.

129 First, we adopted the same size distribution with our previous studies (Matsui et al., 2018; Liu et al., 2022) based on Moteki
130 et al. (2017), abbreviated as Moteki2017 hereafter, which was derived from a power law function to fit the observed
131 anthropogenic iron oxides concentrations within the boundary layer in the outflow of East Asian sources. Note that the
132 observed size-resolved number concentrations were confined within 170 to 2,100 nm in diameter given the detection limit. By
133 extrapolating the observation results, we obtained the mass size distribution between 1 nm and 10,000 nm with negative values
134 excluded. In this case, more than 90% of iron mass was allocated to the size range of 100 nm to 2,500 nm. In addition, we
135 varied the emissions by a factor of two (×0.5 and ×2.0, respectively) in another two parallel experiments to account for the
136 potential uncertainties in iron emission estimates.

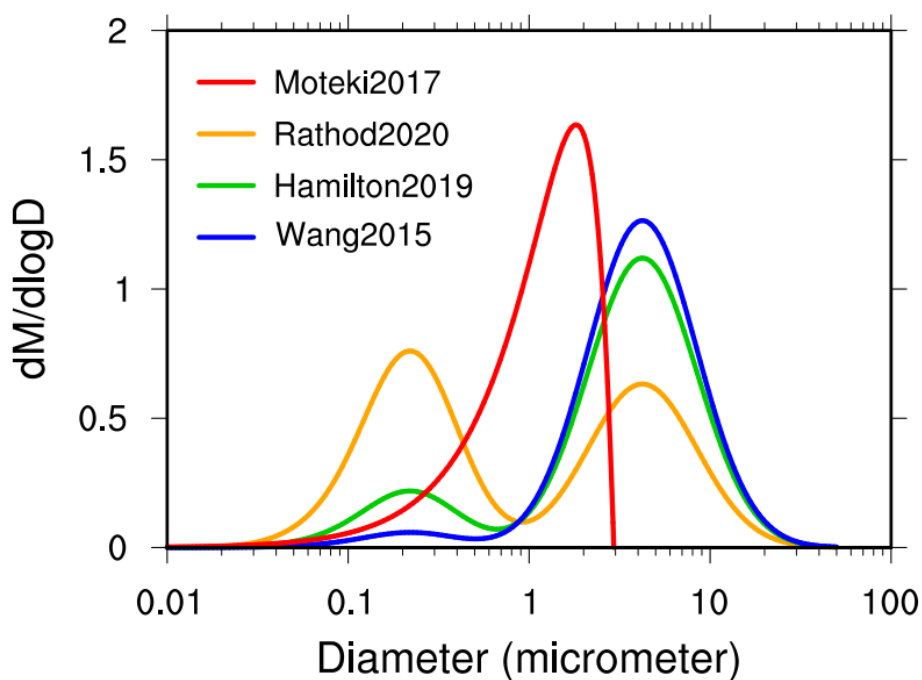
137 The second case was derived from Rathod et al. (2020) (abbreviated as Rathod2020 hereafter). They developed a new
138 mineralogy-based iron emission inventory by introducing more details in anthropogenic sources, especially the inclusion of a
139 metal smelting source. These improvements increase the fine aerosol (less than 1 μm in diameter) fractions by a factor of 10
140 higher than most previous inventories. Consequently, this inventory was characterized with almost equal fractions between
141 fine- and coarse-sized emissions, while previous inventories always applied a much larger fraction for the coarse mode.
142 Consistent with Rathod et al., we allocated 10% and 90% of fine iron mass to the Aitken mode and the accumulation modes
143 of aerosols, respectively.

144 The third case was derived from Hamilton et al. (2019) (abbreviated as Hamilton2019 hereafter). They revised the
145 anthropogenic iron emission inventory based on Luo et al. (2008) (no metal smelting) and showed that the ratio of fine-sized
146 iron mass with that of the coarse-sized was 1:5.6, which resulted in the coarse mode dominating. A similar ratio for

147 anthropogenic iron emissions was applied by Ito (2013). Also, 10% of fine-sized emissions were allocated to the Aitken mode
148 and the remaining 90% to the accumulation mode.

149 The fourth case was derived from Wang et al. (2015) (abbreviated as Wang2015 hereafter). In their combustion-iron inventory,
150 the ratio of fine-mode mass to the coarse mode was as low as 1:24, because only 0.1–0.3 % of iron mass from coal fly ash
151 were emitted in the fine mode. Thus, we allocate 96% of iron in the coarse mode and the remaining 4% in the fine mode.

152 To enable the intercomparison among these cases, we used the global-scale anthropogenic iron emission mass inventory from
153 Rathod et al. (2020) but with different allocations between fine and coarse sizes in each case. The size distribution of
154 anthropogenic iron emission in each case was treated uniformly on a global scale. Therefore, the simulated variability in
155 atmospheric iron input to the ocean between cases should be attributable to iron size distributions rather than emission amount.
156 For the last three cases, we adopted three constant log-normal modes to distribute iron emissions, namely Aitken, accumulation,
157 and coarse modes, with their determining parameters including geometric standard deviations, number mode diameter, and
158 density reported by Hamilton et al. (2019). We then separated these three modes into 12 size bins from 1 nm to 10,000 nm
159 adapted for our size-resolved aerosol modelling. The size distributions of iron from biomass burning and dust sources were
160 consistent with Liu et al. (2022) in all cases. In the following analysis, we grouped the Moteki2017 and Rathod2020 as the
161 fine-sized group while the Hamilton2019 and Wang2015 as the coarse-sized group.



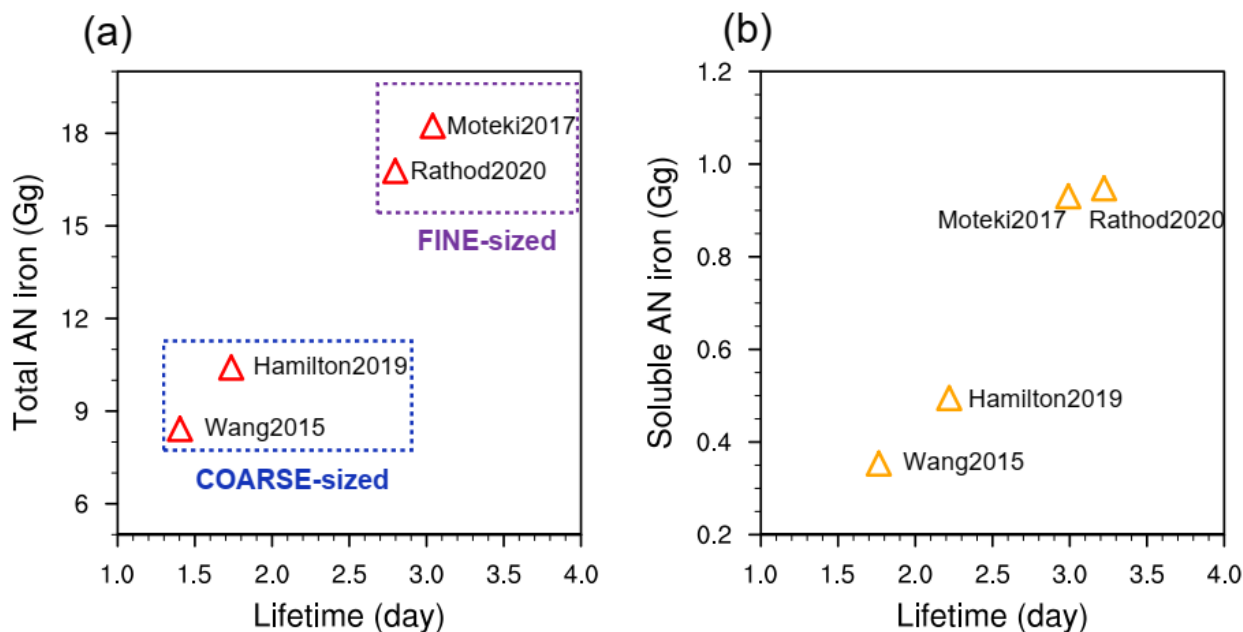
162 **Fig. 1.** Mass size distribution functions for anthropogenic iron emission adopted in four previous studies. The Moteki2017
163 curve was provided by fitting in-situ measurements for iron particles within the range of 170 and 2,100 nm in diameter over
164 East Asia; the Rathod2020 was based on the latest combustion iron emission inventory, with updates on iron estimate in fine-
165 mode sizes (<1 μ m); the Hamilton2019 and Wang2015 cases were modeling studies that assumed most anthropogenic
166 combustion in the coarse-mode bin.
167

168 3. Results and Discussion

170 3.1 Atmospheric iron aerosol concentrations

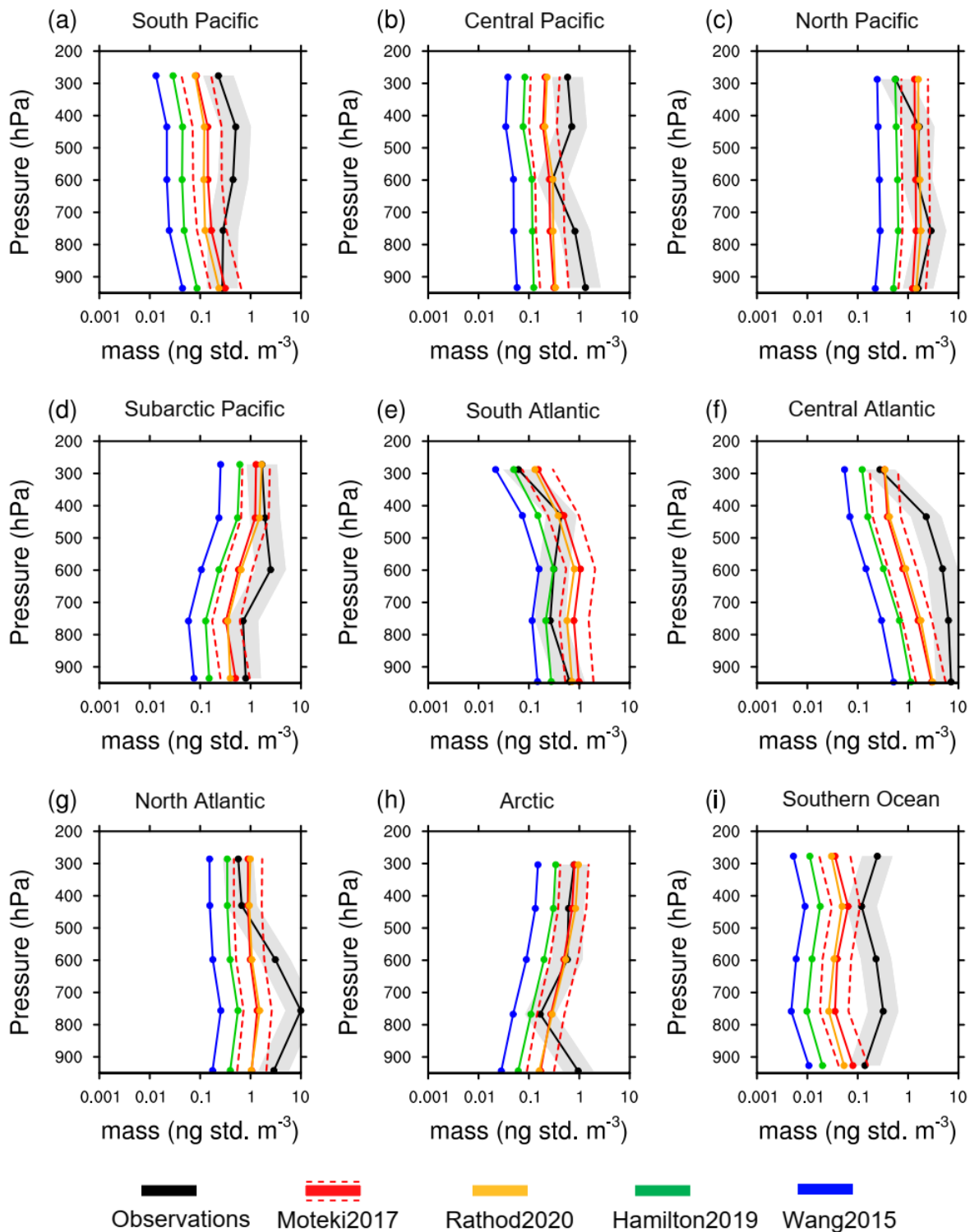
171 We first examined the effect of changes to iron particle size distributions for anthropogenic sources (unless otherwise stated)
172 on the atmospheric iron aerosol burden and its global distributions. Figure 2 illustrates that the global-mean anthropogenic
173 iron lifetimes differ by about a factor of 2 among the four examined cases. Both the Moteki2017 and Rathod2020 cases

174 simulated a lifetime around 3.0 days. In contrast, the Hamilton2019 and Wang2015 cases simulated a lifetime around half as
175 long (between 1.4 and 1.7 days). As only the size distribution is changed in these simulations the change in lifetime is directly
176 linked to the apportionment of mass aerosol between fine and coarse particle size modes. This result is in line with previous
177 reports (Hamilton et al., 2020a), and demonstrates that shifting emitted iron toward fine-sized diminishes atmospheric loss
178 rates of iron aerosols via dry (sedimentation) and wet (precipitation) removal pathways and extends their lifetime.
179 Consequently, given the same emission amount, the atmospheric iron burdens are enhanced, accordingly by approximately a
180 factor of 2 from ~9.0 Gg in the coarse-sized cases (Hamilton2019 and Wang2015) to ~18.0 Gg in the fine-sized cases
181 (Moteki2017 and Rathod2020). In a similar manner, the lifetimes and mass burdens of anthropogenic iron in the soluble form
182 are almost doubled in the fine-sized cases (Fig. 2b). The extended lifetimes also enhance the globally averaged iron solubility
183 (Fig. S2), by allowing more iron subject to aerosol aging and solubilization processes.



184
185 **Fig. 2.** Global anthropogenic iron concentration burdens and lifetimes varied by the emission size distributions. The scatter
186 plots are shown for (a) anthropogenic iron (labeled as AN iron) burden vs. lifetime and (b) soluble anthropogenic iron vs.
187 lifetime. Four representative cases are examined in this work: Moteki2017, Rathod2020, Hamilton2019, and Wang2015. The
188 first two cases are grouped into “FINE-sized” and the other two are grouped into “COARSE-sized”.

189



190

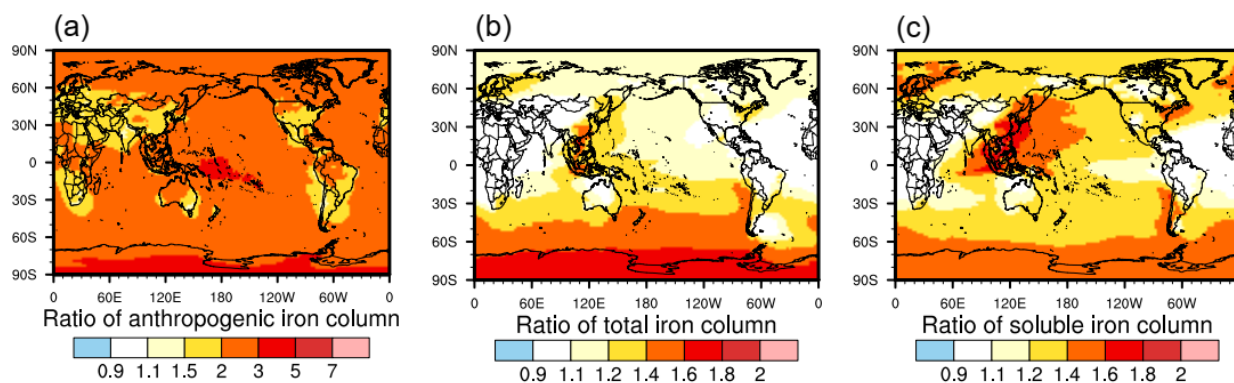
191 **Fig. 3.** Comparison of modelled anthropogenic iron mineral (magnetite) vertical concentration profiles in four cases with
 192 aircraft measurements across global oceans. The flight routes and model-observation sampling methods have been documented
 193 in Lamb et al. (2021) and Liu et al. (2022). The geographical location of each oceanic area is marked in Fig. S1. We also scaled
 194 up and down emission fluxes by a factor of 2 from the Moteki2017 case, respectively, to account for potential uncertainties in
 195 emission estimates (red dashed lines in the panels).

196 To evaluate each iron simulation, we compare simulated aerosol characteristics against global-scale aircraft measurements of
 197 anthropogenic magnetite within nine regions of the troposphere (Fig. 3). We extracted the modeled mass concentrations of
 198 iron aerosols with the size range similar to that of the measurements. Note that magnetite, comprised about 70% of
 199 anthropogenic iron emissions, can be used as an indicator of anthropogenic iron abundance in the atmosphere (Rathod et al.,
 200 2020; Matsui et al., 2018). Despite the same emission fluxes considered in all cases, their simulated magnetite aerosol
 201 concentrations can differ by up to a factor of 10. Specifically, the Moteki2017 and Rathod2020 cases show a much higher

202 performance in reproducing the observed profiles over all ocean basins compared to Hamilton2019 and Wang2015 cases. In
 203 particular, the cases with a more uniformly distributed particle size distribution across modes captures the high concentration
 204 ($>1 \text{ ng m}^{-3}$) in North Pacific, which can be linked to atmospheric plumes transported from East Asia with intensive emission
 205 rates (Seo and Kim, 2023; Moteki et al., 2017). Some underestimations still exist in near-surface or high altitudes. Doubling
 206 the emission fluxes based the Moteki2017 case can appreciably narrow the gaps with the observation (dashed red lines in Fig.
 207 3). In contrast, the coarse-sized dominated simulations (i.e., Hamilton2019 and Wang2015) underrepresents the magnetite
 208 concentrations over global remote oceans, particularly by up to one order of magnitude over the Pacific Ocean. The shorter
 209 lifetimes in this group limit the long-range transport of iron aerosols from continental sources to the remote atmosphere.

210 These results imply that agreement between observations and model simulations can be improved by reducing uncertainties in
 211 the emission inventory and in the long-range transport efficiency associated with representation of iron size distributions.
 212 Moreover, as illustrated in Fig. 3, the variabilities (the ratio between the maximum and minimum) of simulated magnetite
 213 vertical profiles by iron size distribution changes are wider than those by the emission uncertainties, for which emission fluxes
 214 were perturbed by a factor of 2 ($\times 2.0$ and $\times 0.5$, respectively) to test the sensitivity of simulated iron concentrations. We
 215 therefore highlight that in order to observationally constrain iron emissions more realistically in global aerosol simulations, it
 216 is a prerequisite to use a realistic empirical representation of anthropogenic iron aerosol size distributions.

217

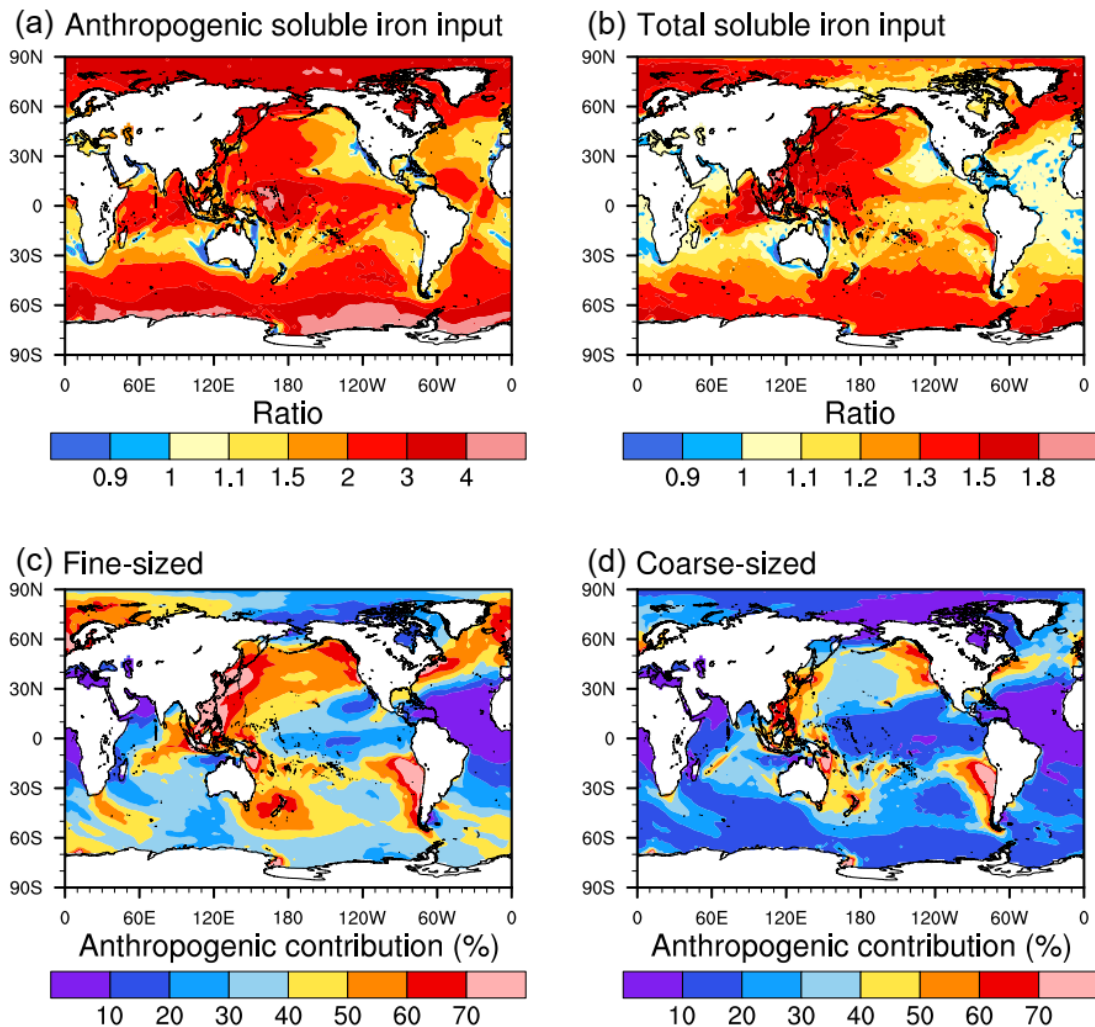


218

219 **Fig. 4.** Global map of variability in yearly averaged iron column concentrations between the fine-sized group and the coarse-
 220 sized group. The variability ratios (fine-sized/coarse-sized) are calculated for (a) anthropogenic iron, (b) total iron, and (c)
 221 soluble iron, respectively. Herein, total iron is a combination of iron from dust, biomass burning, and anthropogenic sources,
 222 the soluble form of which denotes soluble iron. The ratios represent the maximum differences between the fine-sized group
 223 (the Moteki2017 and Rathod2020 cases) and the coarse-sized group (the Hamilton2019 and Wang2015 cases) and indicate the
 224 spread of iron simulations.

225 Our simulations further demonstrate that the representation of iron size distribution shapes the iron aerosol concentrations at a
 226 global scale (Fig. 4). Anthropogenic iron in the fine-sized group shows higher column concentrations by more than a factor of
 227 2 than in the coarse-sized over oceans. The differences (ratios) are larger in those remote oceans compared to source regions
 228 like East Asia, southern Africa and South America, because iron-bearing aerosols in smaller sizes can be transported to a
 229 longer distance. The variability between the two groups is relatively minor for total iron (Fig. 4b), which includes contributions
 230 from dust and biomass burning sources. By contrast, the differences for soluble iron are more pronounced than for total iron
 231 over much of the global Ocean (Fig 4c), because of the higher solubility of anthropogenic iron than dust iron. Over East Asia
 232 and its outflow areas, the rapid aging process in the polluted environments are capable of enhancing iron solubility, particularly
 233 those of anthropogenic origin, and thus amplify the differences of soluble iron concentrations between the fine-sized and
 234 coarse-sized groups (Li et al., 2017; Zhu et al., 2022).

235

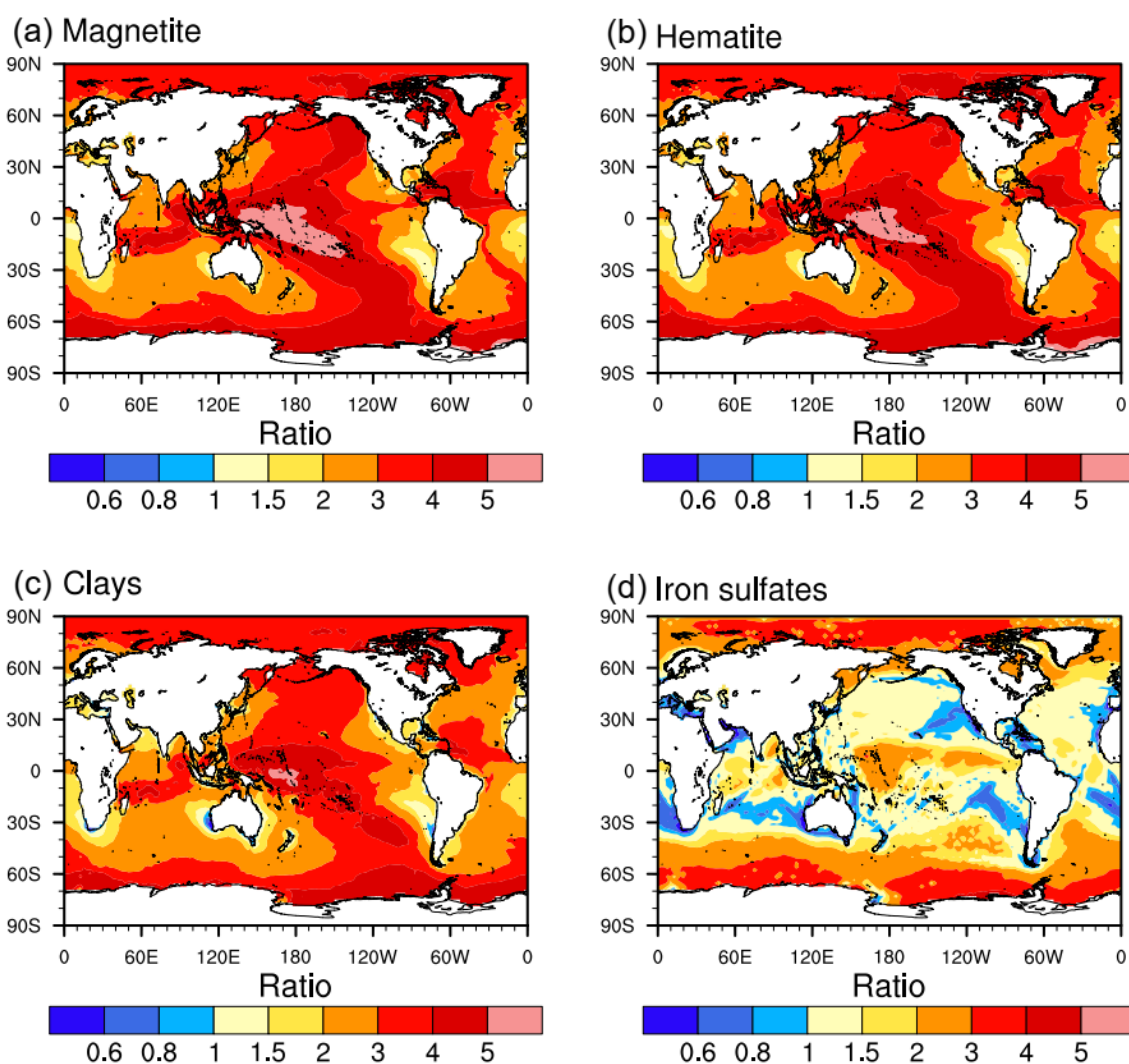


237

238 **Fig. 5.** Comparison of yearly accumulated soluble iron input to the ocean between the fine-sized and coarse-sized cases. Shown
 239 here are (a) the ratio of anthropogenic soluble iron simulated in the fine-sized case to the result of the coarse-sized, (b) the
 240 ratio of total soluble iron, (c) the fractional contribution (in percentage) of anthropogenic emission to total soluble iron input
 241 in the fine-sized case, and (d) the fractional contribution of anthropogenic emission in the coarse-sized case.

242 Next, we examine the extent to which the iron size distributions at emission can alter soluble iron input to the global ocean
 243 basins, which is vital to net primary productivity, especially in the high-nutrient, low-chlorophyll (HNLC) areas (Hamilton et
 244 al., 2022; Moore et al., 2013). As illustrated in Fig. 5, though the global emission and the resulting annual iron (insoluble +
 245 soluble) deposition amount are the same between cases, their geographical distributions vary substantially. Using the ratio of
 246 annual soluble iron deposition in the fine-sized group to that of the coarse-sized as a proxy of the variability, we find the fine-
 247 sized distributions lead to much more soluble iron input to remote ocean basins including North Pacific and Southern Ocean,
 248 by up to a factor of 4 for the anthropogenic sources and 1.5 for the total of all sources (i.e., anthropogenic + fire + dust). Similar
 249 spatial patterns emerge regarding the total iron deposition, suggesting the importance of long-range transport efficiency in
 250 regulating iron distributions (Fig. S3). The variability is negligible in the equatorial and subtropical Atlantic, where dust iron
 251 dominates soluble iron input to this area. The ratios less than 1, indicating reduced deposition fluxes in the fine-sized group,
 252 are found near the continental sources, including western U.S., Australia, and southern Africa, because of the slower deposition
 253 speed. However, in East Asia, which has most intensive anthropogenic iron emissions, the shift toward finer sizes also increase
 254 soluble iron deposition near the sources (e.g., eastern China). This is attributable to the rapid aging processes of the fine-sized
 255 iron in such polluted environment that convert more insoluble iron to its soluble form (Baldo et al., 2022; Zhang et al., 2022).

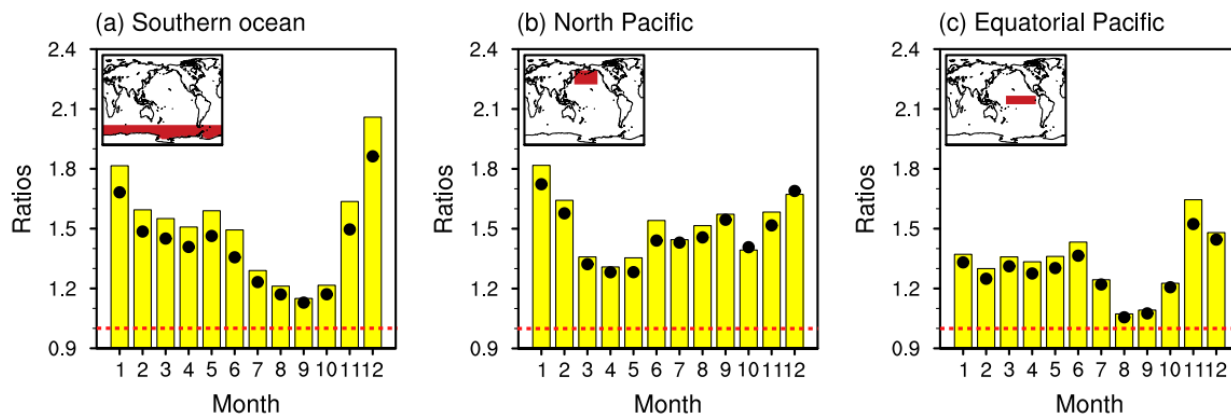
256 The source appointment of soluble iron deposition across ocean basins also varies with iron size distributions (Fig. 5c-d). The
 257 anthropogenic iron source becomes more dominant in North Pacific, North Atlantic, and parts of the Southern Ocean, with its
 258 fractional contribution reaching more than 50% in the fine-sized group compared to that of 30–40% in the coarse-sized. Such
 259 variability is attributable to the enhancement of anthropogenic soluble iron fluxes to those remote oceans by the shift of
 260 anthropogenic iron emission toward finer size bins. Globally, the soluble iron deposition from anthropogenic sources is 55.0
 261 Gg per year for the fine-sized group, larger than that of 35.3 Gg per year for the coarse-sized group. Hence, even though the
 262 same emission is applied in these simulations, the diversity of iron size distributions at emission yields a considerable
 263 variability of soluble iron deposition on a global basis. As discussed earlier, the extended iron lifetime by about a factor to 2
 264 in the fine-sized group allows more iron to be transported to a remote region and simultaneously increases the amount of
 265 atmospheric iron processing and dissolution to a soluble form. Of the total iron deposition, the soluble fraction is thus notably
 266 elevated. We also find that the chemical aging process, as the major source of soluble iron, controls the differences of soluble
 267 iron deposition over remote oceans between the fine-sized and coarse-sized groups (Fig. S4).



268 **Fig. 6.** Ratios of yearly accumulated soluble iron deposition for four anthropogenic iron-containing minerals, comparing fine-
 269 sized and coarse-sized cases.
 270

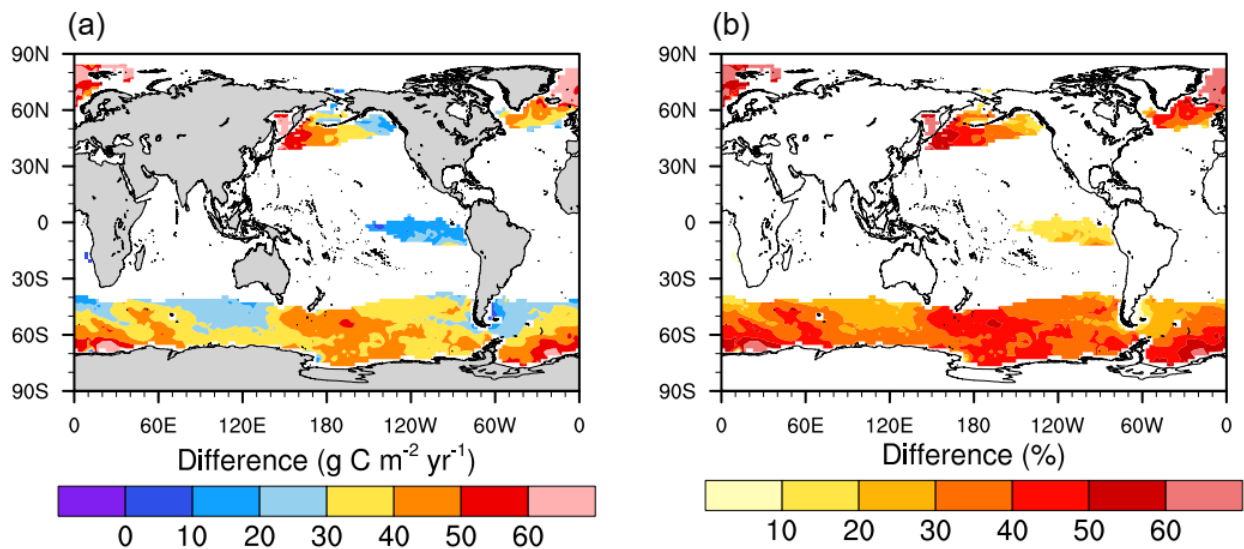
271 In this study, the explicit treatment of anthropogenic iron mineralogy enables us to identify the iron mineral-dependent
 272 variability. We find that for those coming primarily from fossil fuel combustion and iron smelting on land, namely magnetite,
 273 hematite, and clays, the shift of iron emissions toward finer size bins promotes their long-range transport and enhances
 274 corresponding soluble iron deposition to North Pacific, Equatorial Pacific, and Southern Ocean by more than a factor of 4 (Fig.
 275 6a-c). However, the size distribution effects on iron sulfates are pronounced only in the polar areas, which are subject to plumes

276 of middle latitude shipping emissions. In line with previous study (Rathod et al., 2022), the iron sulfates constitute an important
 277 contribution to soluble iron deposition away from major continental sources, predominately associated with shipping emission
 278 over local oceans rather than long-range transport from land (Fig. S5). Hence, the variability induced by iron size distributions
 279 is less remarkable for iron sulfates than for other anthropogenic minerals. These results also suggest that the relative importance
 280 of iron sulfates in total soluble iron deposition to remote oceans is altered by the size distributions of all other iron minerals
 281 that originate from continental sources. Because the size distributions of anthropogenic iron minerals may depend on different
 282 combustion processes, source- and region-specific size distribution representation is desirable in the future work.



283 **Fig. 7.** Differences of monthly total soluble iron deposition between the fine-sized and coarse-sized groups over specific ocean
 284 basins. Only anthropogenic iron emission sizes have been examined here. Histograms describe the ratio of monthly results in
 285 the fine-sized case to that of the coarse-sized for (a) Southern Ocean, (b) North Pacific, and (c) Equatorial Pacific, respectively.
 286 For comparison, black dots describe the ratio of the fine-sized results to that with global anthropogenic emission amount
 287 scaling down by a factor of 2. The ocean basins of interest are indicated at the top-left corner of each panel. The red dashed
 288 lines indicate the ratio of 1.0.
 289

290 It is critical to examine monthly soluble iron availability altered by emission size distributions, because ocean primary
 291 production can respond to iron inputs on the order of days to months (Guieu et al., 2014). From our results in Fig. 7, the
 292 importance of anthropogenic emission size distributions in shifting soluble iron deposition varies by month over potentially
 293 iron-limited ocean basins, i.e., HNLC regions, due to the episodic nature of natural iron sources (dust and wildfire) and their
 294 deposition. For the Southern Ocean, the monthly ratios of the fine-sized case to the coarse-sized span from 1.1 in September
 295 to 2.1 in December (Fig. 7a). The September peak of fire iron (shown in Fig. S6), possibly linked to low precipitation in
 296 southern winter, masks the variability in anthropogenic iron contributions by emission size distributions. Conversely, the
 297 largest difference in December is associated with the lowest contribution of natural sources (Fig. S6). By contrast, the monthly
 298 differences are less fluctuated in North Pacific, ranging between 1.3 and 1.8 (Fig. 7b). Anthropogenic emission dominates
 299 soluble iron throughout the year except in March-May, during which dust storms originating from East Asia frequently occur
 300 and regulate soluble iron inputs to North Pacific. The Equatorial Pacific has the lowest ratio amongst the three regions, because
 301 anthropogenic aerosol bearing plumes rarely arrive in this region and lots of rain out here can efficiently remove aerosols. For
 302 the three ocean basins, such differences related to the emission size treatments are even larger than those by adjusting the iron
 303 emission amount by a factor of 2 with the consideration of emission uncertainty (black dots in Fig. 7). We therefore suggest
 304 that compared with iron emission fluxes, the representation of size distributions for anthropogenic iron is equally or even more
 305 important to the estimation of total soluble iron deposition to remote oceans.



306

307 **Fig. 8.** Difference of marine net primary production sustained by atmospheric soluble iron between two iron size distribution
 308 groups. The panels display (a) absolute differences and (b) percentage differences in net primary production of the fine-sized
 309 group relative to the coarse-sized group. Here, following Rathod et al. (2022), we focus only on the iron-limited ocean basins,
 310 which are defined using a cut-off of nitrate concentrations at surface oceans.

311 We also provide an estimate of the changes in iron-sustained marine net primary production between the finer-sized and coarse-
 312 sized groups (Fig. 8). In line with the distributions of soluble iron deposition, the effects of finer-sized iron distributions can
 313 enhance primary production over remote oceans including the North Pacific Ocean and Southern Ocean as high as 50%.
 314 Considering that anthropogenic iron aerosols may contribute to >10% of the total marine productivity in the North Pacific
 315 Ocean (Rathod et al., 2022; Ito et al., 2020), the representation of their size distributions at emissions, mostly from East Asia,
 316 is particularly important in the Earth system modeling. The evolution of atmospheric iron-aerosol size characteristics and their
 317 emission fluxes can be critical players to ocean carbon sequestration from past to future. Hamilton et al. (2020) found that
 318 historical air pollution controls has cut down anthropogenic emission amounts of particles in coarse sizes, in turn elevating the
 319 mass fraction of finer-sized iron particles and thus the overall lifetime of atmospheric iron. Hence, the complex interactions of
 320 iron and the Earth system is linked to human activity effects on soluble iron availability to ocean basins.

321

322 4. Conclusion

323 This study explores the extent to which iron size distribution at emission, specifically from anthropogenic sources, alters
 324 estimates of soluble iron deposition to the open ocean. A global microphysical, size-resolved aerosol model is used to simulate
 325 the iron cycle, involving emission, atmospheric processing, and deposition on a global scale. The model treats iron mineralogy,
 326 size evolution, and chemical aging processes during atmospheric transport, which enables the investigation on the relationship
 327 between iron size distributions and iron long-range transport and subsequent deposition. We test four representative size
 328 distribution schemes for anthropogenic iron sources employed in previous studies.

329 We find that allocating a more balanced fraction of iron aerosol at emission into particle sizes less than $1 \mu\text{m}$, results in a longer
 330 atmospheric lifetime and mass burden of total iron aerosols by about a factor of 2 compared to a coarse-sized dominated case,
 331 primarily associated with the decreased loss rates via dry and wet removal processes. The evaluation of anthropogenic iron
 332 aerosols against the global-scale observation dataset reveals that despite the same emission fluxes considered in all cases, their
 333 simulated magnetite aerosol concentrations differ by up to a factor of 10, while the higher fine-sized cases agree better with
 334 the observations. It is therefore necessary to accurately represent iron size distributions in order to constrain iron emission
 335 fluxes more realistically with aerosol simulations and observations (Liu et al., 2022). Our simulations show that the resulting

336 annual soluble iron deposition differs by up to a factor of 1.5 over remote oceans including the North Pacific Ocean and
337 Southern Ocean, because the fine-sized group allows more iron to be transported to a long distance with enhanced atmospheric
338 processing. More importantly, the monthly soluble iron deposition, which is relevant to ocean primary production responses
339 over days to months, would be enhanced by 110% and 80% in the fine-sized case over the Southern Ocean and North Pacific
340 Ocean, respectively. Such differences are similar to or even larger than those with the consideration of emission uncertainty,
341 suggesting the equally important role of iron size distribution treatment.

342 This study unravels the critical role of iron size distributions in shaping atmospheric soluble iron inputs to global oceans,
343 especially to the remote regions. However, the realistic understanding of iron emission size distributions is still inadequate
344 given limited observation data. Targeted in-site measurements on iron aerosol size along with its mass and solubility at source
345 areas are highly desirable. Higher resolution models with finer grids and detailed microphysics are useful to explore iron
346 aerosol deposition and chemical aging processes at regional scales. Furthermore, our finding may be extended to other key
347 trace elements of importance to ocean biogeochemistry, like copper, manganese, and phosphorus.

348

349 **Competing interests:** The authors declare that they have no conflict of interest.

350 **Data availability:** The model data used to generate the figures can be available upon request.

351 **Code availability:** The CESM source code is publicly available from NCAR at: <https://www.cesm.ucar.edu/>.

352 **Acknowledgement**

353 This study was supported by the Ministry of Education, Culture, Sports, Science, and Technology and the Japan Society for
354 the Promotion of Science (MEXT/JSPS) KAKENHI Grants (JP19H04253, JP19H05699, JP19KK0265, JP20H00196,
355 JP20H00638, JP22H03722, JP22F22092, JP23H00515, JP23H00523, JP23K18519, JP23K24976, and JP24H02225); by the
356 MEXT Arctic Challenge for Sustainability II (ArCS II) Project (JPMXD1420318865); and by the Environment Research and
357 Technology Development Fund 2–2003 (JPMEERF20202003) and 2–2301 (JPMEERF20232001) of the Environmental
358 Restoration and Conservation Agency. Mingxu Liu was supported by special fund of State Key Joint Laboratory of
359 Environmental Simulation and Pollution Control (24Y03ESPCP) and JSPS Postdoctoral Fellowships for Research in Japan
360 (Standard). DSH was supported by NASA (Proposal Number: 22-IDS22-0027). We acknowledged the NASA Radiation
361 Sciences Program, the NASA Upper Atmosphere Research Program, and the NOAA Atmospheric Composition and Climate
362 Program for providing the aircraft observational data.

363

364 **References:**

- 365 Albani, S., Mahowald, N. M., Perry, A. T., Scanza, R. A., Zender, C. S., Heavens, N. G., Maggi, V., Kok, J. F.,
366 and Otto-Bliesner, B. L.: Improved dust representation in the Community Atmosphere Model, *J. Adv. Model.*
367 *Earth Syst.*, 6, 541-570, <https://doi.org/10.1002/2013MS000279>, 2014.
- 368 Baldo, C., Ito, A., Krom, M. D., Li, W., Jones, T., Drake, N., Ignatyev, K., Davidson, N., and Shi, Z.: Iron from
369 coal combustion particles dissolves much faster than mineral dust under simulated atmospheric acidic
370 conditions, *Atmos. Chem. Phys.*, 22, 6045-6066, 10.5194/acp-22-6045-2022, 2022.
- 371 Bergas-Massó, E., Gonçalves Ageitos, M., Myriokefalitakis, S., Miller, R. L., van Noije, T., Le Sager, P., Montan
372 é Pinto, G., and Pérez García-Pando, C.: Pre-Industrial, Present and Future Atmospheric Soluble Iron
373 Deposition and the Role of Aerosol Acidity and Oxalate Under CMIP6 Emissions, *Earth's Future*, 11,
374 10.1029/2022ef003353, 2023.

375 Conway, T. M., Hamilton, D. S., Shelley, R. U., Aguilar-Islas, A. M., Landing, W. M., Mahowald, N. M., and John,
376 S. G.: Tracing and constraining anthropogenic aerosol iron fluxes to the North Atlantic Ocean using iron
377 isotopes, *Nat Commun*, 10, 2628, 10.1038/s41467-019-10457-w, 2019.

378 Gliß, J., Mortier, A., Schulz, M., Andrews, E., Balkanski, Y., Bauer, S. E., Benedictow, A. M. K., Bian, H., Checa-
379 Garcia, R., Chin, M., Ginoux, P., Griesfeller, J. J., Heckel, A., Kipling, Z., Kirkevåg, A., Kokkola, H., Laj, P.,
380 Le Sager, P., Lund, M. T., Lund Myhre, C., Matsui, H., Myhre, G., Neubauer, D., van Noije, T., North, P.,
381 Olivié, D. J. L., Rémy, S., Sogacheva, L., Takemura, T., Tsigaridis, K., and Tsyro, S. G.: AeroCom phase III
382 multi-model evaluation of the aerosol life cycle and optical properties using ground- and space-based remote
383 sensing as well as surface in situ observations, *Atmos. Chem. Phys.*, 21, 87-128, 10.5194/acp-21-87-2021,
384 2021.

385 Guieu, C., Aumont, O., Paytan, A., Bopp, L., Law, C. S., Mahowald, N., Achterberg, E. P., Marañón, E., Salihoglu,
386 B., Crise, A., Wagener, T., Herut, B., Desboeufs, K., Kanakidou, M., Olgun, N., Peters, F., Pulido-Villena, E.,
387 Tovar-Sanchez, A., and Völker, C.: The significance of the episodic nature of atmospheric deposition to Low
388 Nutrient Low Chlorophyll regions, *Global Biogeochemical Cycles*, 28, 1179-1198,
389 <https://doi.org/10.1002/2014GB004852>, 2014.

390 Hamilton, D. S., Scanza, R. A., Rathod, S. D., Bond, T. C., Kok, J. F., Li, L., Matsui, H., and Mahowald, N. M.:
391 Recent (1980 to 2015) Trends and Variability in Daily-to-Interannual Soluble Iron Deposition from Dust,
392 Fire, and Anthropogenic Sources, *Geophysical Research Letters*, 47, e2020GL089688,
393 10.1029/2020gl089688, 2020a.

394 Hamilton, D. S., Scanza, R. A., Feng, Y., Guinness, J., Kok, J. F., Li, L., Liu, X., Rathod, S. D., Wan, J. S., Wu,
395 M., and Mahowald, N. M.: Improved methodologies for Earth system modelling of atmospheric soluble iron
396 and observation comparisons using the Mechanism of Intermediate complexity for Modelling Iron (MIMI
397 v1.0), *Geosci. Model Dev.*, 12, 3835-3862, 10.5194/gmd-12-3835-2019, 2019.

398 Hamilton, D. S., Moore, J. K., Arneeth, A., Bond, T. C., Carslaw, K. S., Hantson, S., Ito, A., Kaplan, J. O., Lindsay,
399 K., Nieradzik, L., Rathod, S. D., Scanza, R. A., and Mahowald, N. M.: Impact of Changes to the Atmospheric
400 Soluble Iron Deposition Flux on Ocean Biogeochemical Cycles in the Anthropocene, *Global Biogeochemical
401 Cycles*, 34, e2019GB006448, 10.1029/2019gb006448, 2020b.

402 Hamilton, D. S., Perron, M. M. G., Bond, T. C., Bowie, A. R., Buchholz, R. R., Guieu, C., Ito, A., Maenhaut, W.,
403 Myriokefalitakis, S., Olgun, N., Rathod, S. D., Schepanski, K., Tagliabue, A., Wagner, R., and Mahowald, N.
404 M.: Earth, Wind, Fire, and Pollution: Aerosol Nutrient Sources and Impacts on Ocean Biogeochemistry, 14,
405 303-330, 10.1146/annurev-marine-031921-013612, 2022.

406 Ito, A.: Global modeling study of potentially bioavailable iron input from shipboard aerosol sources to the ocean,
407 *Global Biogeochemical Cycles*, 27, 1-10, <https://doi.org/10.1029/2012GB004378>, 2013.

408 Ito, A.: Atmospheric Processing of Combustion Aerosols as a Source of Bioavailable Iron, *Environ. Sci. Technol.
409 Lett.*, 2, 70-75, 10.1021/acs.estlett.5b00007, 2015.

410 Ito, A., Ye, Y., Yamamoto, A., Watanabe, M., and Aita, M. N.: Responses of ocean biogeochemistry to atmospheric
411 supply of lithogenic and pyrogenic iron-containing aerosols, *Geol. Mag.*, 157, 741-756,
412 10.1017/S0016756819001080, 2020.

413 Ito, A., Myriokefalitakis, S., Kanakidou, M., Mahowald, N. M., Scanza, R. A., Hamilton, D. S., Baker, A. R.,
414 Jickells, T., Sarin, M., Bikkina, S., Gao, Y., Shelley, R. U., Buck, C. S., Landing, W. M., Bowie, A. R., Perron,
415 M. M. G., Guieu, C., Meskhidze, N., Johnson, M. S., Feng, Y., Kok, J. F., Nenes, A., and Duce, R. A.:
416 Pyrogenic iron: The missing link to high iron solubility in aerosols, *Sci. Adv.*, 5, eaau7671,
417 10.1126/sciadv.aau7671, 2019.

418 Jickells, T. and Moore, C. M.: The Importance of Atmospheric Deposition for Ocean Productivity, *Annu. Rev.
419 Ecol. Evol. Syst.*, 46, 481-501, 10.1146/annurev-ecolsys-112414-054118, 2015.

420 Jickells, T. D., An, Z. S., Andersen, K. K., Baker, A. R., Bergametti, G., Brooks, N., Cao, J. J., Boyd, P. W., Duce,
421 R. A., Hunter, K. A., Kawahata, H., Kubilay, N., laRoche, J., Liss, P. S., Mahowald, N., Prospero, J. M.,
422 Ridgwell, A. J., Tegen, I., and Torres, R.: Global Iron Connections Between Desert Dust, Ocean
423 Biogeochemistry, and Climate, *Science*, 308, 67, 10.1126/science.1105959, 2005.

424 Kawai, K., Matsui, H., and Tobo, Y.: High Potential of Asian Dust to Act as Ice Nucleating Particles in Mixed-
425 Phase Clouds Simulated With a Global Aerosol-Climate Model, *J. Geophys. Res.-Atmos*, 126,
426 e2020JD034263, <https://doi.org/10.1029/2020JD034263>, 2021.

427 Kok, J. F.: A scaling theory for the size distribution of emitted dust aerosols suggests climate models underestimate
428 the size of the global dust cycle, *Proceedings of the National Academy of Sciences of the United States of
429 America*, 108, 1016, 10.1073/pnas.1014798108, 2011.

430 Lamb, K. D., Matsui, H., Katich, J. M., Perring, A. E., Spackman, J. R., Weinzierl, B., Dollner, M., and Schwarz,
431 J. P.: Global-scale constraints on light-absorbing anthropogenic iron oxide aerosols, *npj Clim. Atmos. Sci.*, 4,
432 10.1038/s41612-021-00171-0, 2021.

433 Li, W., Xu, L., Liu, X., Zhang, J., Lin, Y., Yao, X., Gao, H., Zhang, D., Chen, J., Wang, W., Harrison, R. M.,
434 Zhang, X., Shao, L., Fu, P., Nenes, A., and Shi, Z.: Air pollution–aerosol interactions produce more
435 bioavailable iron for ocean ecosystems, *Sci. Adv.*, 3, e1601749, 10.1126/sciadv.1601749, 2017.

436 Liu, M. and Matsui, H.: Improved Simulations of Global Black Carbon Distributions by Modifying Wet
437 Scavenging Processes in Convective and Mixed-Phase Clouds, *J. Geophys. Res.-Atmos*, 126, e2020JD033890,
438 <https://doi.org/10.1029/2020JD033890>, 2021.

439 Liu, M. and Matsui, H.: Secondary Organic Aerosol Formation Regulates Cloud Condensation Nuclei in the Global
440 Remote Troposphere, *Geophysical Research Letters*, 49, 10.1029/2022gl100543, 2022.

441 Liu, M., Matsui, H., Hamilton, D. S., Lamb, K. D., Rathod, S. D., Schwarz, J. P., and Mahowald, N. M.: The
442 underappreciated role of anthropogenic sources in atmospheric soluble iron flux to the Southern Ocean, *npj*
443 *Clim. Atmos. Sci.*, 5, 10.1038/s41612-022-00250-w, 2022.

444 Liu, X., Easter, R. C., Ghan, S. J., Zaveri, R., Rasch, P., Shi, X., Lamarque, J. F., Gettelman, A., Morrison, H., Vitt,
445 F., Conley, A., Park, S., Neale, R., Hannay, C., Ekman, A. M. L., Hess, P., Mahowald, N., Collins, W., Iacono,
446 M. J., Bretherton, C. S., Flanner, M. G., and Mitchell, D.: Toward a minimal representation of aerosols in
447 climate models: description and evaluation in the Community Atmosphere Model CAM5, *Geosci. Model Dev.*,
448 5, 709-739, 10.5194/gmd-5-709-2012, 2012.

449 Longo, A. F., Feng, Y., Lai, B., Landing, W. M., Shelley, R. U., Nenes, A., Mihalopoulos, N., Violaki, K., and
450 Ingall, E. D.: Influence of Atmospheric Processes on the Solubility and Composition of Iron in Saharan Dust,
451 *Environmental Science & Technology*, 50, 6912-6920, 10.1021/acs.est.6b02605, 2016.

452 Luo, C., Mahowald, N., Bond, T., Chuang, P. Y., Artaxo, P., Siefert, R., Chen, Y., and Schauer, J.: Combustion
453 iron distribution and deposition, *Global Biogeochemical Cycles*, 22, GB1012,
454 <https://doi.org/10.1029/2007GB002964>, 2008.

455 Mahowald, N., Albani, S., Kok, J. F., Engelstaeder, S., Scanza, R., Ward, D. S., and Flanner, M. G.: The size
456 distribution of desert dust aerosols and its impact on the Earth system, *Aeolian Res.*, 15, 53-71,
457 <https://doi.org/10.1016/j.aeolia.2013.09.002>, 2014.

458 Mahowald, N. M., Hamilton, D. S., Mackey, K. R. M., Moore, J. K., Baker, A. R., Scanza, R. A., and Zhang, Y.:
459 Aerosol trace metal leaching and impacts on marine microorganisms, *Nat. Commun.*, 9, 2614,
460 10.1038/s41467-018-04970-7, 2018.

461 Mahowald, N. M., Engelstaedter, S., Luo, C., Sealy, A., Artaxo, P., Benitez-Nelson, C., Bonnet, S., Chen, Y.,
462 Chuang, P. Y., Cohen, D. D., Dulac, F., Herut, B., Johansen, A. M., Kubilay, N., Losno, R., Maenhaut, W.,
463 Paytan, A., Prospero, J. M., Shank, L. M., and Siefert, R. L.: Atmospheric Iron Deposition: Global Distribution,
464 Variability, and Human Perturbations, *Annual Review of Marine Science*, 1, 245-278,
465 10.1146/annurev.marine.010908.163727, 2009.

466 Matsui, H.: Development of a global aerosol model using a two-dimensional sectional method: 1. Model design, *J.*
467 *Adv. Model. Earth Syst.*, 9, 1921-1947, 10.1002/2017ms000936, 2017.

468 Matsui, H. and Liu, M.: Importance of Supersaturation in Arctic Black Carbon Simulations, *Journal of Climate*, 34,
469 7843-7856, 10.1175/jcli-d-20-0994.1, 2021.

470 Matsui, H. and Mahowald, N.: Development of a global aerosol model using a two-dimensional sectional method:
471 2. Evaluation and sensitivity simulations, *J. Adv. Model. Earth Syst.*, 9, 1887-1920, 10.1002/2017ms000937,
472 2017.

473 Matsui, H. and Moteki, N.: High sensitivity of Arctic black carbon radiative effects to subgrid vertical velocity in
474 aerosol activation, *Geophysical Research Letters*, 47, e2020GL088978, 10.1029/2020GL088978, 2020.

475 Matsui, H., Mori, T., Ohata, S., Moteki, N., Oshima, N., Goto-Azuma, K., Koike, M., and Kondo, Y.: Contrasting
476 source contributions of Arctic black carbon to atmospheric concentrations, deposition flux, and atmospheric
477 and snow radiative effects, *Atmos. Chem. Phys. Discuss.*, 2022, 1-31, 10.5194/acp-2021-1091, 2022.

478 Matsui, H., Mahowald, N. M., Moteki, N., Hamilton, D. S., Ohata, S., Yoshida, A., Koike, M., Scanza, R. A., and
479 Flanner, M. G.: Anthropogenic combustion iron as a complex climate forcer, *Nat. Commun.*, 9, 1593,
480 10.1038/s41467-018-03997-0, 2018.

481 Meskhidze, N., Völker, C., Al-Abadleh, H. A., Barbeau, K., Bressac, M., Buck, C., Bundy, R. M., Croot, P., Feng,
482 Y., Ito, A., Johansen, A. M., Landing, W. M., Mao, J., Myriokefalitakis, S., Ohnemus, D., Pasquier, B., and
483 Ye, Y.: Perspective on identifying and characterizing the processes controlling iron speciation and residence
484 time at the atmosphere-ocean interface, *Marine Chemistry*, 217, 103704,
485 <https://doi.org/10.1016/j.marchem.2019.103704>, 2019.

486 Moore, C. M., Mills, M. M., Arrigo, K. R., Berman-Frank, I., Bopp, L., Boyd, P. W., Galbraith, E. D., Geider, R.
487 J., Guieu, C., Jaccard, S. L., Jickells, T. D., La Roche, J., Lenton, T. M., Mahowald, N. M., Marañón, E.,
488 Marinov, I., Moore, J. K., Nakatsuka, T., Oschlies, A., Saito, M. A., Thingstad, T. F., Tsuda, A., and Ulloa,
489 O.: Processes and patterns of oceanic nutrient limitation, *Nat. Geosci.*, 6, 701-710, 10.1038/ngeo1765, 2013.

490 Moore, J. K., Doney, S. C., Glover, D. M., and Fung, I. Y.: Iron cycling and nutrient-limitation patterns in surface
 491 waters of the World Ocean, *Deep Sea Research Part II: Topical Studies in Oceanography*, 49, 463-507,
 492 [https://doi.org/10.1016/S0967-0645\(01\)00109-6](https://doi.org/10.1016/S0967-0645(01)00109-6), 2001.

493 Moteki, N., Adachi, K., Ohata, S., Yoshida, A., Harigaya, T., Koike, M., and Kondo, Y.: Anthropogenic iron oxide
 494 aerosols enhance atmospheric heating, *Nat. Commun.*, 8, 15329, 10.1038/ncomms15329, 2017.

495 Myriokefalitakis, S., Gröger, M., Hieronymus, J., and Döschner, R.: An explicit estimate of the atmospheric nutrient
 496 impact on global oceanic productivity, *Ocean Sci.*, 16, 1183-1205, 10.5194/os-16-1183-2020, 2020.

497 Myriokefalitakis, S., Ito, A., Kanakidou, M., Nenes, A., Krol, M. C., Mahowald, N. M., Scanza, R. A., Hamilton,
 498 D. S., Johnson, M. S., Meskhidze, N., Kok, J. F., Guieu, C., Baker, A. R., Jickells, T. D., Sarin, M. M., Bikkina,
 499 S., Shelley, R., Bowie, A., Perron, M. M. G., and Duce, R. A.: Reviews and syntheses: the GESAMP
 500 atmospheric iron deposition model intercomparison study, *Biogeosciences*, 15, 6659-6684, 10.5194/bg-15-
 501 6659-2018, 2018.

502 Okin, G. S., Baker, A. R., Tegen, I., Mahowald, N. M., Dentener, F. J., Duce, R. A., Galloway, J. N., Hunter, K.,
 503 Kanakidou, M., Kubilay, N., Prospero, J. M., Sarin, M., Surapipith, V., Uematsu, M., and Zhu, T.: Impacts of
 504 atmospheric nutrient deposition on marine productivity: Roles of nitrogen, phosphorus, and iron, *Global
 505 Biogeochemical Cycles*, 25, <https://doi.org/10.1029/2010GB003858>, 2011.

506 Rathod, S. D., Hamilton, D. S., Mahowald, N. M., Klimont, Z., Corbett, J. J., and Bond, T. C.: A Mineralogy-
 507 Based Anthropogenic Combustion-Iron Emission Inventory, *J. Geophys. Res.-Atmos*, 125, e2019JD032114,
 508 10.1029/2019jd032114, 2020.

509 Rathod, S. D., Hamilton, D. S., Li, L., Mahowald, N. M., Matsui, H., Pierce, J. R., and Bond, T. C.: Atmospheric
 510 Radiative and Oceanic Biological Productivity Responses to Increasing Anthropogenic Combustion-Iron
 511 Emission in the 1850–2010 Period, *Geophys. Res. Lett.*, 49, 10.1029/2022gl099323, 2022.

512 Seo, H. and Kim, G.: Anthropogenic Iron Invasion into the Ocean: Results from the East Sea (Japan Sea), *Environ.
 513 Sci. Technol.*, 57, 10745-10753, 10.1021/acs.est.3c01084, 2023.

514 Shi, J., Guan, Y., Ito, A., Gao, H., Yao, X., Baker, A. R., and Zhang, D.: High Production of Soluble Iron Promoted
 515 by Aerosol Acidification in Fog, *Geophysical Research Letters*, 47, 10.1029/2019gl086124, 2020.

516 Shi, Z., Krom, M. D., Jickells, T. D., Bonneville, S., Carslaw, K. S., Mihalopoulos, N., Baker, A. R., and Benning,
 517 L. G.: Impacts on iron solubility in the mineral dust by processes in the source region and the atmosphere: A
 518 review, *Aeolian Res.*, 5, 21-42, <https://doi.org/10.1016/j.aeolia.2012.03.001>, 2012.

519 Solmon, F., Chuang, P. Y., Meskhidze, N., and Chen, Y.: Acidic processing of mineral dust iron by anthropogenic
 520 compounds over the north Pacific Ocean, *J. Geophys. Res.-Atmos*, 114,
 521 <https://doi.org/10.1029/2008JD010417>, 2009.

522 Tagliabue, A., Bowie, A. R., Boyd, P. W., Buck, K. N., Johnson, K. S., and Saito, M. A.: The integral role of iron
 523 in ocean biogeochemistry, *Nature*, 543, 51-59, 10.1038/nature21058, 2017.

524 Wang, R., Balkanski, Y., Boucher, O., Bopp, L., Chappell, A., Ciais, P., Hauglustaine, D., Peñuelas, J., and Tao,
 525 S.: Sources, transport and deposition of iron in the global atmosphere, *Atmos. Chem. Phys.*, 15, 6247-6270,
 526 10.5194/acp-15-6247-2015, 2015.

527 Westberry, T. K., Behrenfeld, M. J., Shi, Y. R., Yu, H., Remer, L. A., and Bian, H.: Atmospheric nourishment of
 528 global ocean ecosystems, 380, 515-519, doi:10.1126/science.abq5252, 2023.

529 Zender, C. S., Bian, H., and Newman, D.: Mineral Dust Entrainment and Deposition (DEAD) model: Description
 530 and 1990s dust climatology, *J. Geophys. Res.-Atmos*, 108, 4416, <https://doi.org/10.1029/2002JD002775>,
 531 2003.

532 Zhang, H., Li, R., Dong, S., Wang, F., Zhu, Y., Meng, H., Huang, C., Ren, Y., Wang, X., Hu, X., Li, T., Peng, C.,
 533 Zhang, G., Xue, L., Wang, X., and Tang, M.: Abundance and Fractional Solubility of Aerosol Iron During
 534 Winter at a Coastal City in Northern China: Similarities and Contrasts Between Fine and Coarse Particles, *J.
 535 Geophys. Res.-Atmos*, 127, e2021JD036070, <https://doi.org/10.1029/2021JD036070>, 2022.

536 Zhang, H., Li, R., Huang, C., Li, X., Dong, S., Wang, F., Li, T., Chen, Y., Zhang, G., Ren, Y., Chen, Q., Huang,
 537 R., Chen, S., Xue, T., Wang, X., and Tang, M.: Seasonal variation of aerosol iron solubility in coarse and fine
 538 particles at an inland city in northwestern China, *Atmos. Chem. Phys.*, 23, 3543-3559, 10.5194/acp-23-3543-
 539 2023, 2023.

540 Zhang, L., Gong, S., Padro, J., and Barrie, L.: A size-segregated particle dry deposition scheme for an atmospheric
 541 aerosol module, *Atmospheric Environment*, 35, 549-560, [https://doi.org/10.1016/S1352-2310\(00\)00326-5](https://doi.org/10.1016/S1352-2310(00)00326-5),
 542 2001.

543 Zhu, Y., Li, W., Wang, Y., Zhang, J., Liu, L., Xu, L., Xu, J., Shi, J., Shao, L., Fu, P., Zhang, D., and Shi, Z.: Sources
 544 and processes of iron aerosols in a megacity in Eastern China, *Atmos. Chem. Phys.*, 22, 2191-2202,
 545 10.5194/acp-22-2191-2022, 2022.

546

547